Spurious-Free Dynamic Range in Photonic Integrated Circuit Filters with Semiconductor Optical Amplifiers

Robert S. Guzzon, Erik J. Norberg, and Larry A. Coldren, *Fellow, IEEE*

(*Invited Paper*)

***Abstract*— Among other advantages, radio-frequency (RF) signal processing in the optical domain using photonic integrated circuits (PICs) offers unprecedented bandwidth and tunability. However, modern RF-photonic link applications demand PICs with high spurious-free dynamic range (SFDR). The SFDR of active PICs integrating semiconductor optical amplifiers (SOAs) is limited by amplified spontaneous emission noise and distortion caused by four-wave mixing. Here, we derive an analytical model for the SFDR of SOAs, and extend it to PICs with arbitrary transfer functions integrating many SOAs. The model is general and applicable to any photonic signal-processing circuit operating in the linear amplification regime below saturation. We show analytically the importance of SFDR-driven photonic design over noise-figure-driven design. Using this model, we explore the SFDR of coupled-ring bandpass filters integrated on a high saturation power integration platform and show SFDR as high as 117.0 dB $\cdot$ Hz$^{2/3}$ for filters with bandwidths in the 1–2 GHz range. We show how the material parameters and PIC design determine the SFDR. Tradeoffs between SFDR and filter bandwidth, extinction, and stopband roll-off are investigated.**

***Index Terms*— Integrated optoelectronics, microwave photonics, optical filters, photonic integrated circuits, semiconductor optical amplifiers.**

I. Introduction

OPTICAL analog signal processing at telecom wavelengths for RF applications has attracted attention due to the advantages provided by RF photonic links. Radio over fiber (RoF) systems provide low-loss transmission, wide bandwidth, and immunity to electromagnetic interference (EMI) [1]. Within such systems, photonic filters can provide widely tunable and high quality factor (Q) filters with operating bandwidths not achievable in current RF electronic technology for new applications demanding center frequencies up to 100 GHz [2]. In addition, analog signal processing in the optical domain can potentially provide size, weight, and power (SWaP) dividends [3].

Manuscript received August 1, 2011; revised October 18, 2011; accepted October 22, 2011. Date of current version January 24, 2012. This work was supported in part by DARPA under Program PhASER. A portion of this work was completed in the UCSB nanofabrication facility, part of the National Science Foundation-National Nanotechnology Infrastructure Network.

The authors are with the Department of Electrical and Computer Engineering and Department of Materials, University of California Santa Barbara, Santa Barbara, CA 93106 USA (e-mail: guzzon@ece.ucsb.edu; norberg@ece.ucsb.edu; coldren@ece.ucsb.edu).

Color versions of one or more of the figures in this paper are available online at http://ieeexplore.ieee.org.

Digital Object Identifier 10.1109/JQE.2011.2174618

Microwave photonic filtering can be achieved in a variety of ways using bulk optics [4], and more recently, photonic integrated circuits (PICs) [5]–[10]. PICs can capitalize on SWaP and stability improvements over bulk optical solutions while providing a high level of programmability and tunability to the filtering application. However, RF link performance must not be compromised by the photonic subsystem. Traditionally, signal fidelity is quantitatively described by the system spurious-free dynamic range (SFDR). The theoretical and experimental SFDR limitations in RF photonic links involving passive PIC filters have been evaluated [2], [11]. In these systems, filters introduce optical loss, but do not add noise or signal distortion. Therefore, SFDR is limited by the modulation and detection nonlinearities; laser, shot, and receiver noise; and link gain.

Recently, we have described and evaluated active PIC filters in the InGaAsP/InP material system [9]. Fig. 1 displays a fabricated PIC filter and measured bandpass spectra. Integrated semiconductor optical amplifiers (SOAs) provide high tunability to active filters and compensate for passive waveguide loss within ring structures, allowing for the synthesis of near-ideal filter shapes incorporating high Q resonators. With intra-ring gain, filter design relies less on the exact specification of inter-ring coupling values, and becomes more flexible. Filter bandwidth can be set independently of pole magnitude, guaranteeing a flat-topped filter design regardless of bandwidth. In addition, filters can be designed with passband gain. Fabrication in the InGaAsP/InP material system is also advantageous for integration with other active photonic components such and transmitters and receivers. These benefits come at the expense of added amplified spontaneous emission (ASE) noise [12] and nonlinearities stemming from the four-wave mixing (FWM) phenomenon created by carrier population oscillations (CPO) [13].

A full theoretical SFDR treatment has been conducted for a single SOA operating in the nonlinear large-signal regime [14]. In this paper, we extend ASE and CPO theory to determine the PIC-limited SFDR of a coherent heterodyne RF photonic link. This general model describes any PIC integrating SOAs that operate below saturation. Here, we outline the model and apply it to PIC bandpass filters utilizing low-gain SOAs. When integrated on a high-saturation power integration platform [15], the model predicts SFDR as high as 117.0 dB $\cdot$ Hz$^{2/3}$ for

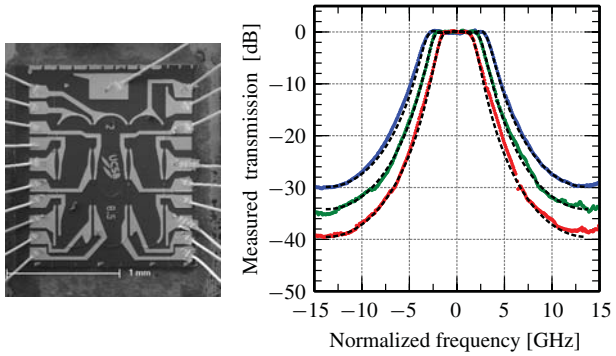

Fig. 1. (a) SEM picture of a fabricated and wire-bonded third-order coupled ring filter. (b) Third-order bandpass filters measured in the RF domain, normalized in frequency and amplitude for clarity. These filters were measured to have between 0.0 and 5.0 dB optical passband gain. The dotted lines are a theoretical fit. More details in [9].

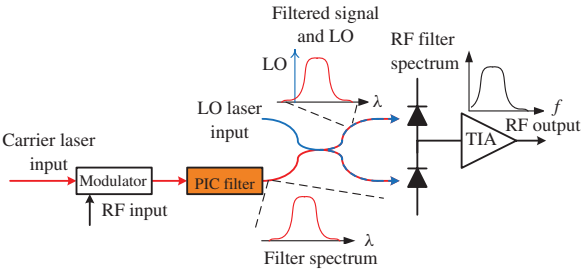

Fig. 2. RF photonic link including modulator, PIC filter, and balanced receiver. The optical signal is in red, RF electrical signals in black, and LO in blue.

a second-order coupled-ring bandpass filter with a 1.75 GHz bandwidth. Results show clear trade-offs between linearity and filter bandwidth, extinction, and roll-off, while shedding light on optimal filter design. The model also shows that noise figure alone may not provide the optimal design of an analog optical link, and that SFDR provides a more useful metric.

II. Theoretical Background

Fig. 2 schematically represents a coherent heterodyne RF photonic link. In such a system, a strong local oscillator (LO) downconverts the PIC-filtered optical signal through a balanced detection receiver. The link could be over a long distance in fiber, or be contained on a single PIC depending on the application.

A. SFDR in Terms of Optical Powers

The SFDR of a system describes the range over which a signal remains above the noise level, while spurious distortion power remains below the noise level. In particular, the third-order intermodulation distortion (IMD) products between two input tones $2f_2 - f_1$ and $2f_1 - f_2$ are of prime interest because of their proximity to the signal band. The two-tone SFDR can be written as the ratio of the third-order electrical intercept power to the electrical noise power in the receiver [16]

$$SFDR = \left[\frac{P_{\mathrm{OIP3,elec}}}{N}\right]^{\frac{2}{3}} = \left[\frac{\langle i^2_{\mathrm{OIP3}}\rangle}{\langle i^2_N\rangle}\right]^{\frac{2}{3}} \quad (1)$$

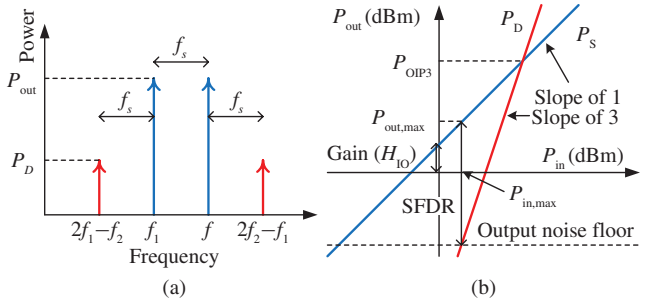

Fig. 3. Schematic representation of two-tone SFDR showing. (a) Relationship of the fundamental tones with separation frequency f_s to the IMD tones $2f_2 - f_1$ and $2f_1 - f_2$. (b) Signal (P_S) and IMD distortion power (P_D) as a function of input signal power. SFDR and the output intercept point are labeled on this dB-dB plot.

where $P_{\mathrm{OIP3,elec}}$ is the output third-order intercept electrical power, N is the electrical noise power, $\langle i^2_{\mathrm{OIP3}}\rangle$ is the output third-order intercept mean-square current, and $\langle i^2_N\rangle$ is the noise equivalent mean-square current. A schematic representation of the two-tone SFDR is presented in Fig. 3. Since the impedance seen by all currents in the receiver are equal, signal and noise quantities are written above in terms of mean-square currents, where the angle brackets denote averaging. In order to concentrate on the effect of the PIC on SFDR, we will assume an ideal transmitter and receiver where laser RIN and thermal noise do not dominate. In a real system, this may not be the case. In particular, the receiver noise may be appreciable. However, the aim of this paper is not to investigate the SFDR of a realistic link, but look at how a PIC with integrated SOAs impacts a link independently of other noise sources. In such a case, noise in a heterodyne RF photonic link with optical amplification is dominated by shot noise and LO-ASE beat noise. The mean squared shot noise current at the receiver where the LO power is much greater than the signal power is given by [17]

$$\left\langle i^2_{\mathrm{shot}}\right\rangle = 2qRP_{\mathrm{LO}}\Delta f \quad (2)$$

where q is the electron charge, $R = q/\hbar\omega$ is the responsivity of an ideal detector, P_{LO} is the optical power of the LO, and Δf is the bandwidth of the receiver. Only the LO optical power appears in (2) because the LO power is assumed to be much larger than the signal and noise. The LO-ASE beat noise for single-sideband detection is given by [17]

$$\left\langle i^2_{\mathrm{LO-ASE}}\right\rangle = 2R^2P_{\mathrm{LO}}S_{\mathrm{ASE}}\Delta f \quad (3)$$

where S_{ASE} is the power spectral density of ASE in the mode. Single-sideband detection is assumed because the noise spectrum is filtered by the PIC such that only one sideband is dominant. This results in the pre-factor of 2 rather than 4 in Eq. (3). The mean-squared third-order intercept current is given by

$$\left\langle i^2_{\mathrm{OIP3}}\right\rangle = 2R^2P_{\mathrm{LO}}P_{\mathrm{OIP3}} \quad (4)$$

where P_{OIP3} is the power at the third-order optical output intercept point (OIP3). Thus, in an optical heterodyne system where the LO power is much greater than the signal power, the SFDR can be written in terms of optical powers. Substituting

(2), (3), and (4) into (1), the SFDR in terms of optical powers is

$$SFDR = \left[\frac{P_{\mathrm{OIP3}}}{(S_{\mathrm{ASE}} + \hbar\omega)\Delta f}\right]^{\frac{2}{3}} \tag{5}$$

SFDR can be written in terms of noise factor as

$$SFDR = \left[\frac{P_{\mathrm{OIP3}}}{H_{\mathrm{IO}}\hbar\omega F_n \Delta f}\right]^{\frac{2}{3}} \tag{6}$$

where H_{IO} is the power transfer function from input to output, and the noise factor is given by [17]

$$F_n = \frac{S_{\mathrm{ASE}}}{H_{\mathrm{IO}}\hbar\omega} + \frac{1}{H_{\mathrm{IO}}}. \tag{7}$$

The first term represents LO-ASE beat noise, and the second term represents the shot noise contribution. SFDR is typically multiplied by $\Delta f^{2/3}$ and quoted on a receiver bandwidth independent dB scale as $\mathrm{dB} \cdot \mathrm{Hz}^{2/3}$.

SFDR is a range over which the signal power can swing without inducing distortion and without falling below the noise floor. For each SFDR, it is convenient to calculate the maximum optical input power or output power of the PIC needed to take advantage of the full dynamic range. These maximum optical powers can be deduced from Fig. 3(b) as:

$$P_{\mathrm{out,max}} = \frac{P_{\mathrm{OIP3}}}{\sqrt{SFDR}} \tag{8}$$

$$P_{\mathrm{in,max}} = \frac{P_{\mathrm{OIP3}}}{H_{\mathrm{IO}}\sqrt{SFDR}}. \tag{9}$$

B. ASE Noise Generation in a Single SOA

To determine the ASE noise at the receiver, we first look at the noise generated by a single SOA. Starting with the spontaneous photon density rate equation for a traveling wave amplifier, writing it as a differential equation with respect to position in the SOA, and writing it in terms of power spectral density we have [12]

$$\frac{dS_{\mathrm{ASE}}}{dz} = (\Gamma g - \alpha_i)S_{\mathrm{ASE}} + \Gamma g n_{sp}\hbar\omega \tag{10}$$

where S_{ASE} is the ASE power spectral density in the mode, Γg is the modal gain, α_i is the modal loss, and n_{sp} is the population inversion factor. Solving the differential equation and integrating over the length of the SOA, L [12]

$$S_{\mathrm{ASE}} = \frac{n_{sp}\hbar\omega}{\zeta}(G-1) = N_{\mathrm{mat}}(G-1) \tag{11}$$

where G is the single-pass power gain given by $G = e^{(\Gamma g - \alpha_i)L}$, and $\zeta = (\Gamma g - \alpha_i)/\Gamma g$. For a particular material and waveguide design, and at a particular operation point (current density) and wavelength, n_{sp}, ζ, and $\hbar\omega$ are constant, and are therefore lumped into the material noise parameter N_{mat}. The total ASE power in the mode is simply $P_{\mathrm{ASE}} = S_{\mathrm{ASE}}\Delta f$ where Δf is the ASE bandwidth.

C. Intermodulation Distortion Generation in a Single SOA

The theory of FWM through CPO in SOAs has been studied extensively in the past [13]–[15], [18]–[22]. When certain assumptions are made, an analytical solution can be attained for the intermodulation distortion power generated by an SOA [13], [19]. First, a small-signal approach is taken, where the input tones are assumed to be much larger than the distortion products, and modulation of the carrier density is small compared to its average. Also, higher-order modulation of the carrier density by beating of input tones with distortion products can be ignored. Finally, the carrier density is assumed to be constant along the length of the SOA. These assumptions are valid for a system operating in the linear amplification regime, well below saturation. This is the regime in which we hope to operate. [13], [19] also make the additional assumption of high single-pass gain. The filters presented here often incorporate SOAs with very low single-pass gain, rendering this assumption invalid. Here, we present a new result that does not require high single-pass gain. Additionally, [13], [19] utilize the slowly-varying envelope approximation to simplify the second order differential wave equation to a first order differential equation. Here, we analytically solve the second order differential equation directly and derive an equation for the optical power generated in a third-order IMD tone by two equal input tones.

Starting with the carrier density rate equation

$$\frac{dN}{dt} = \frac{I_a}{qV} - \frac{N}{\tau} - \frac{g(N)}{\hbar\omega}|E|^2 \tag{12}$$

where N is the carrier density, I_a is the current into the active region, V is the active volume, τ is the carrier lifetime, $g(N)$ is the material gain, and E is the electric field in the active region, normalized by the factor $\sqrt{n\epsilon_0 c/2}$ such that $I = |E|^2$ is the optical intensity in the active region. Using the saturation intensity in the active region $I_S = \hbar\omega/a\tau$ and $g(N) = a(N - N_0)$ where a is the differential gain and N_0 is the transparency current density, the rate equation can be written in time-harmonic form as

$$j\omega N I_S \tau = \frac{I_a I_S \tau}{qV} - N I_S - (N - N_0)|E|^2. \tag{13}$$

The electric field for 2 input tones of equal amplitude is given by

$$E = E_0 + E_1 = E_e\left(e^{j\omega_0 t} + e^{j\omega_1 t}\right) \tag{14}$$

where $E_e = E_{in}e^{(\Gamma g - \alpha_i)z/2}$ is the electric field envelope along the SOA and E_{in} is the input electric field magnitude. The carrier density can be separated into an average value and a value modulated at the difference frequency between the input tones

$$N = \bar{N} + \Delta N\left(e^{j(\omega_1 - \omega_0)t} + e^{-j(\omega_1 - \omega_0)t}\right). \tag{15}$$

Substituting (14) and (15) into (13) and solving for $\bar{N}$ and ΔN gives

$$\bar{N} = \frac{I_a I_S \tau/qV + 2N_0 E_e^2}{I_S + 2E_e^2} \tag{16}$$

$$\Delta N = \frac{-(\bar{N} - N_0)E_e^2}{(1 + j\omega_s\tau)I_S + 2E_e^2} \tag{17}$$

where $\omega_s = \omega_1 - \omega_0$ is the separation between the input tones. Now, using the wave equation, the distortion power generated and amplified in each IMD tone can be determined. Keeping only the field component at the IMD frequency, the wave equation for the IMD tone, E_D, in the propagation (z) direction can be written [18]

$$\frac{d^2E_D}{dz^2} + \tilde{k}_D^2 E_D = \Gamma a(\alpha + j\zeta)\Delta N k_D E_e e^{jk_D z} \tag{18}$$

where α is the linewidth enhancement factor, $\tilde{k}_D = k_D - j(\Gamma g - \alpha_i)/2$ is the complex propagation constant for the distortion field, and k_D is the real part of the propagation constant. Now, substituting (16) into (17), the result into (18), using $g = a(N - N_0)$, and keeping only the dominant term in the denominator, the wave equation becomes

$$\frac{d^2E_D}{dz^2} + \tilde{k}_D^2 E_D = \frac{-\Gamma g(\alpha + j\zeta)k_D E_e^3 e^{jk_D z}}{(1 + j\omega_s\tau)I_S}. \tag{19}$$

Solving (19) with the boundary conditions $E_D(0) = 0$ and $E'_D(0) = 0$, using $I = |E|^2$ and the optical power in the mode $P = I A_{\text{active}}/\Gamma$, and keeping only dominant terms, the total distortion power at the output of the SOA is

$$\begin{aligned} P_D(L) &= \frac{(1 + \alpha^2/\zeta^2)}{4(1 + (\omega_s\tau)^2)} \frac{P_{in}^3}{P_S^2} G\,[G-1]^2 \\ &= A_{\text{mat}} P_{in}^3 G\,[G-1]^2 \end{aligned} \tag{20}$$

where P_{in} is the input power of each tone, P_S is the modal saturation power, and $G = e^{(\Gamma g - \alpha_i)L}$ is the single-pass power gain. For a particular material and waveguide design, and at a particular operating current density, α, ζ, P_S, and τ are constant, and are therefore lumped into the material parameter A_{mat}. According to Eq. (20), IMD power is inversely proportional to P_S^2. It is therefore important for best SFDR performance to operate SOAs at their optimal current density where the peak gain and peak saturation power are obtained. Eq. (20) then relates the third-order IMD power generated in each SOA to the optical power at the input of the SOA and the total SOA gain. Contrary to [13] and [19], this result is valid for low single-pass gain where the assumption $G \gg 1$ is not valid. The presence of the $[G-1]^2$ term in (20) and the $G-1$ term in (11) indicates a low-gain operation regime where high SFDR can be obtained. Photonic microwave filters integrating SOAs in rings such as the ones presented in this paper operate within such a regime.

The IMD output intercept power is related to the distortion power by

$$P_{\text{OIP3}} = \left[\frac{(H_{\text{IO}}P_{in})^3}{P_D}\right]^{\frac{1}{2}} \tag{21}$$

where H_{IO} is the power transfer function from input to output, which is simply equal to G in the case of a single SOA. If we define a unit-less distortion

$$D = \frac{P_D}{A_{\text{mat}} P_{in}^3} = G[G-1]^2. \tag{22}$$

P_{OIP3} can be written independently of P_{in}

$$P_{\text{OIP3}} = \left[\frac{H_{\text{IO}}^3}{DA_{\text{mat}}}\right]^{\frac{1}{2}}. \tag{23}$$

Eq. (11) and (23) relate the noise and OIP3 of an SOA to its material parameters N_{mat} and A_{mat} and its single-pass gain, G. In a more complex system involving multiple SOAs and multiple waveguide paths, S_{ASE} and D can be determined for each SOA, and the contribution summed at the receiver.

D. Noise and Distortion in a System with Multiple SOAs

In a PIC integrating multiple SOAs and waveguide paths like the ones schematically shown in Fig. 4(a) and (b), each SOA generates noise and distortion at the receiver depending on its total gain and location in the PIC. The single-pass SOA gain is determined by active material length. The location of an SOA in the PIC determines the wavelength-dependent transfer function from the input to the SOA, and the transfer function from the SOA to the output. The input-to-SOA transfer function determines P_{in} for that SOA, and the SOA-to-output transfer function determines the wavelength-dependent amplification or loss incurred by the IMD power and ASE power as they propagate to the receiver. From Eq. (11), the contribution to ASE noise at the receiver from the n^{th} SOA can be written

$$S_{\text{ASE,n}}(\lambda) = N_{\text{mat}}(G_n - 1)H_{SO,n}(\lambda) \tag{24}$$

where $H_{SO,n}(\lambda)$ is the SOA-to-output power transfer function for the n^{th} SOA. Then, the total ASE power is incoherently summed at the receiver

$$S_{\text{ASE,total}}(\lambda) = \sum_{n=1}^{N} S_{\text{ASE,n}}(\lambda). \tag{25}$$

Extending Eq. (22), the contribution to IMD at the receiver from the n^{th} SOA can be written

$$D_n(\lambda) = G_n[G_n - 1]^2 H_{IS,n}^3(\lambda)H_{SO,n}(\lambda) \tag{26}$$

where $H_{IS,n}(\lambda)$ is the input-to-SOA power transfer function for the n^{th} SOA. Since the distortion is created from a coherent signal, it is likewise coherent, and is created in-phase in each SOA. Therefore, the total IMD is coherently summed at the receiver

$$D_{\text{total}}(\lambda) = \left[\sum_{n=1}^{N} \sqrt{D_n(\lambda)}\right]^2. \tag{27}$$

The summation in (27) accounts for the in-phase coherent addition of the distortion created by each SOA. Eq. (27) is equivalent to simply adding the IMD electric fields from each SOA in-phase.

Once the ASE and IMD power contributions from each SOA are deduced at the output, the OIP3 power [Eq. (23)] and SFDR [Eq. (5)] are calculated as a function of wavelength. This "spot-SFDR" output reflects the noise and the distortion generated by two closely-spaced tones [$\omega_s\tau \ll 1$ in Eq. (20)] at each frequency. This is a different approach than the conventional method for reporting SFDR, which assumes constant distortion and noise across the receiver bandwidth. However, for wide bandwidth signals, the frequency dependence of distortion and noise should be considered [16]. The actual SFDR for a signal falling in the bandwidth of the filter depends on the signal bandwidth and placement in the filter passband,

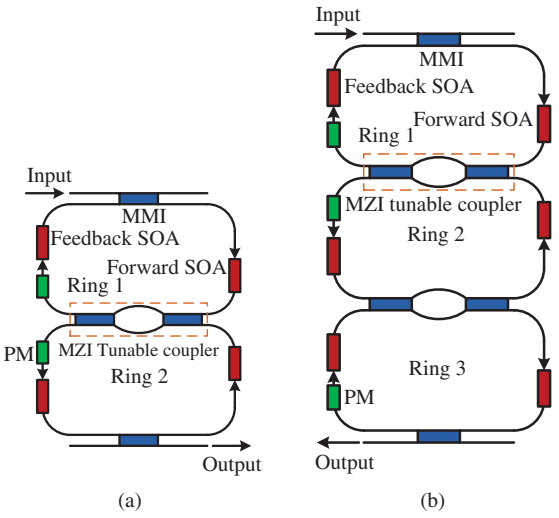

Fig. 4. Schematic representation of (a) second-order and (b) third-order coupled-ring filter. MMIs are in blue, SOAs in red, and phase modulators (PMs) in green.

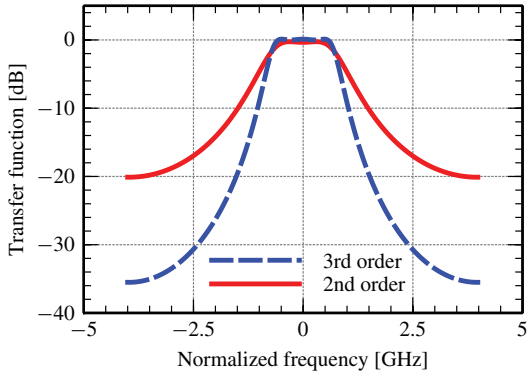

Fig. 5. Optical power transfer functions of second and third-order bandpass filters utilizing the same ring length and inter-ring coupling value. The filters are not normalized, but are shown at the passband gain which produces the optimal SFDR. Pole magnitudes were chosen to produce flat-topped bandpass filter responses [9].

and is a complex function of many-tone interactions [16]. However, the minimum and maximum spot-SFDR across the filter bandwidth provide an upper and lower bound for the third-order SFDR of an arbitrary signal.

E. Example: SOA on a Waveguide

The simple example of a single SOA on a waveguide demonstrates the importance of considering SFDR as a figure of merit in lightwave systems as opposed to relying solely on noise figure. We will consider two cases: 1) a lossy waveguide with an SOA at the beginning of the waveguide, and 2) a lossy waveguide with an SOA at the end of the waveguide. Using the equations in the preceding sections, it can be shown that the SFDR of case 2 is equal to

$$SFDR_2 = \left[\frac{n_{sp}/\zeta(G-1)+1/H_{SO}}{n_{sp}/\zeta(G-1)+1}\right]^{\frac{2}{3}} SFDR_1 \qquad (28)$$

where H_{SO} is the SOA-to-output transfer function in case 1 and G is the SOA gain for both cases. $G > 1$, and for a lossy waveguide, $0 < H_{SO} < 1$, so the prefactor on the right hand side of Eq. (28) is always greater than 1. Therefore, the SFDR of case 2 is always greater than the SFDR of case 1, implying that for an arbitrary amount of lossy waveguide and an arbitrary amount of gain, it is always better to place the gain at the end of the waveguide. This is contrary to the typical noise-figure-based design rule, which is to place gain elements at the beginning of a string of lossy elements in order to minimize noise figure [17]. Eq. 28 is valid as long as the signal remains above the shot noise limit, which is the case for the PIC systems described in the next sections.

III. Simulation of SFDR in a PIC Filter

A. Description of the PIC Filter

PICs incorporating SOAs can provide high-quality photonic signal processing for RF applications. As described above, noise and distortion generated in the SOAs negatively impact signal fidelity. Using the results from Section II, we developed a simulation package that calculates the PIC-limited SFDR of an ideal RF-photonic link. The results are shown in Figs. 7–10. The simulation models an RF-photonic link utilizing coherent detection via optical heterodyne downconversion, and assumes an LO power much greater than the signal, allowing for a simple expression of SFDR in terms of optical powers [Eq. (5)]. Using the transfer functions of a PIC, the simulation package determines the PIC-limited SFDR of any design operating in the linear amplification regime. The SFDR in a real system may be lower due to laser RIN and receiver noise, and depends on the particular transmitter and receiver utilized, and on the optical LO power. Coupled-ring filters like the one described in [9] are adept at creating high-quality bandpass filters [23]. Here, we investigate the SFDR of such systems. [9] describes how the input-to-output transfer functions of coupled-ring PIC filters are calculated. Similarly, input-to-SOA and SOA-to-output transfer functions can be derived using Mason's Formula [24]. Fig. 4(a) and (b) schematically represent the second and third-order coupled ring filters investigated here. Fig. 5 shows their transfer functions.

From Eq. (11) and (20), it is clear that minimizing total SOA gain in a PIC filter while maintaining the desired functionality is crucial for obtaining high SFDR. Within rings, SOAs compensate for loss in order to obtain pole magnitudes sufficient for synthesis of flat-topped bandpass filters. Therefore, low waveguide propagation loss and coupler insertion loss directly translate to higher SFDR. In general, trade-offs exist between filter shape ideality and SFDR. High-quality flat-topped bandpass filters with high extinction and fast stop-band roll-off require high-order filters with high pole magnitudes [23]. Increasing the filter order (number of rings) increases waveguide propagation loss and in turn requires more gain. In addition, higher pole magnitudes require higher SOA gain. Increasing both filter order and pole magnitudes therefore decreases SFDR.

In order to reduce filter bandwidth, ring delay lengths must be increased and/or pole magnitudes must be increased. Adding waveguide length adds propagation loss. Therefore narrow bandwidth filters produce a lower SFDR per unit

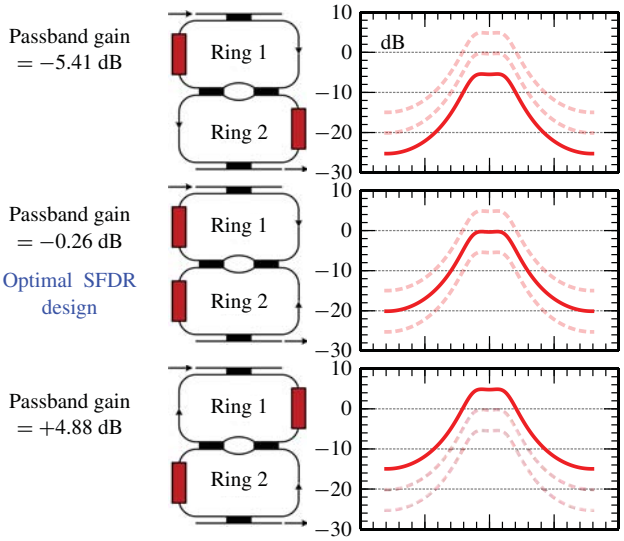

Fig. 6. Schematic representation of a second-order coupled ring bandpass filter with certain SOA configurations and the resulting transfer function. (a) Lowest passband gain configuration, with both SOAs in the feedback segments. (b) Optimal SFDR configuration with a passband gain near 0 dB. The ring 1 SOA is in the feedback segment and the ring 2 SOA is in the forward segment. (c) Highest passband gain configuration, with both SOAs in the forward waveguide segments.

TABLE I
SIMULATION PARAMETERS

Symbol	Parameter	Value
n_{sp}	Population inversion factor	1.3
N_{mat}	ASE material parameter [15]	1.78×10^{-9} J
A_{mat}	IMD material parameter [15]	127 W^{-2}
P_S	Saturation power [15]	19.1 dBm
n_g	Group index	3.78
λ	Center wavelength	1.55 μm
α_{ip}	Passive waveguide loss [15]	1.0 cm^{-1}
α_i	Active waveguide loss [15]	2.0 cm^{-1}
Γg	Modal gain [15]	19.7 cm^{-1}

of bandwidth than wide bandwidth filters. Filter geometry can also affect the filter SFDR. A coupled-ring system is investigated here, because such systems inherently require less SOA gain than cascaded-ring systems (systems where there is no feedback between rings). A fraction of the input power to each ring is discarded in a cascaded-ring system in the input coupler of each ring [9]. This excess loss decreases SFDR compared to coupled-ring systems.

B. Simulation Results and Discussion

Table I displays the simulation parameters used in the following results. All parameters are kept constant unless otherwise noted. The material constant A_{mat} is extracted from IMD measurements of a new high-dynamic range InGaAsP/InP integration platform [15]. This platform integrates deeply-etched waveguides and low-confinement-factor quantum-well (QW) SOAs to allow for high SFDR PICs with tight waveguide bends and low waveguide propagation loss. The filters in [9] are integrated on a similar platform. Using Γg and α_i from [15], we assumed $n_{sp} = 1.3$ [25] in order to find N_{mat}. As a check of the IMD theory, the linewidth enhancement factor

TABLE II
2nd-ORDER FILTER SIMULATION PARAMETERS

Symbol	Parameter	Value
p_{r1}, p_{r2}	Intrinsic pole magnitude 1, 3 [9]	0.58
C	Inter-ring power coupling	15%
	Filter 3 dB bandwidth	1.75 GHz
	Maximum extinction ratio	19.8 dB
	Maximum roll-off	11.7 dB/GHz
	MMI insertion loss	0.5 dB
	Ring length	1.0 cm
	Feedback to forward waveguide ratio	10.0

TABLE III
3rd-ORDER FILTER SIMULATION PARAMETERS

Symbol	Parameter	Value
p_{r1}, p_{r3}	Intrinsic pole magnitude 1, 3 [9]	0.61
p_{r2}	Intrinsic pole magnitude 2 [9]	0.85
C	Inter-ring power coupling	15%
	Filter 3 dB bandwidth	1.55 GHz
	Maximum extinction ratio	35.6 dB
	Maximum roll-off	27.7 dB/GHz
	MMI insertion loss	0.5 dB
	Ring length	1.0 cm
	Feedback to forward waveguide ratio	10.0

is determined from A_{mat} in (20) to be $\alpha = 1.37$. This is low for InGaAsP/InP-based QW devices, but is within an order of magnitude of the expected value [26], showing that the theory of IMD generation is reasonably accurate. With the A_{mat} parameter extracted from real measurements, we expect the results presented here to be realistic.

In the following sections we present simulation results for second and third-order coupled-ring bandpass filters. Each SFDR result is accompanied by other system parameters that result from the particular configuration of SOAs and waveguides used for that filter. For instance, in a coupled-ring system, each ring has a forward and feedback segment of waveguide. In order to create a certain filter shape, the pole magnitude of each ring is set by the amount of gain and loss in the ring [9]. However, the IMD, ASE, and passband gain characteristics of the filter are dependent on the distribution of waveguide length and SOA gain between the forward and feedback segments. The shape of the filter does not change as long as the total gain and loss in each ring remains the same. However, SFDR is dependent on the IMD, ASE, and total input-to-output transfer function (H_{IO}). An optimal SFDR can be found, or passband gain modified, by adjusting the distribution of waveguide and SOA between the forward and feedback segments of each ring. The "shape" of the filter is here defined as the dB transfer function. Fig. 6 shows several SOA configurations that result in the same second-order filter shape, but different levels of passband gain. As SOA distribution is varied from fully in the feedback segment to fully in the forward segment in either ring, the passband gain of the filter will increase. The filter shape will not change however, as long as the total SOA gain in the ring remains the same. The distribution of waveguide length between the forward and feedback segments also affects the passband gain. The feedback to forward ratio given in Tables II, III is defined as the ratio of the feedback waveguide length to the forward waveguide length. As this ratio is varied from small to large values, the passband gain of the filter will increase (without any change

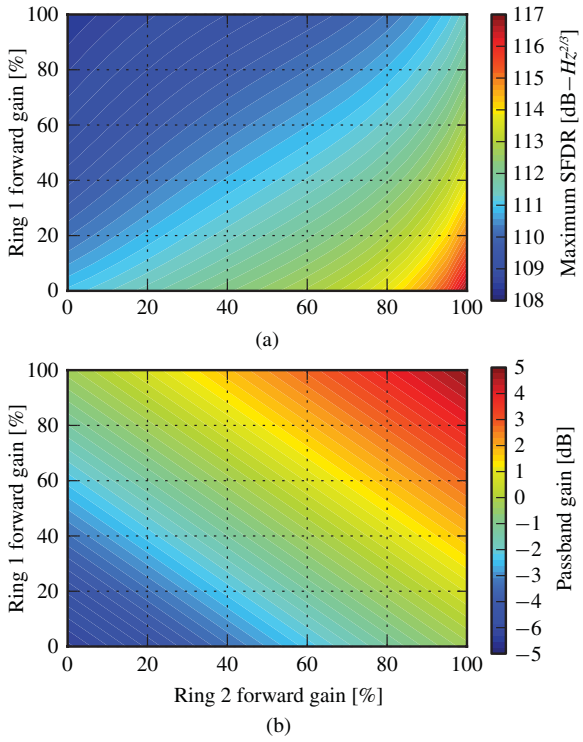

Fig. 7. (a) Peak SFDR and (b) peak passband gain across the 3 dB bandwidth of a second-order bandpass filter as a function of the distribution of SOA gain between the forward and feedback segments of rings 1 and 2. Total SOA gain per ring is held constant in order to produce the same filter shape for all points on the map. 100% forward gain means that all of the SOA is located in the forward segment, and none is located in the feedback segment. There is a clear optimal SFDR point when the ring 1 SOA is fully in the feedback segment and the ring 2 SOA is fully in forward segment. The passband gain can be swept from −5.4 dB to +4.9 dB by adjusting the SOA placement.

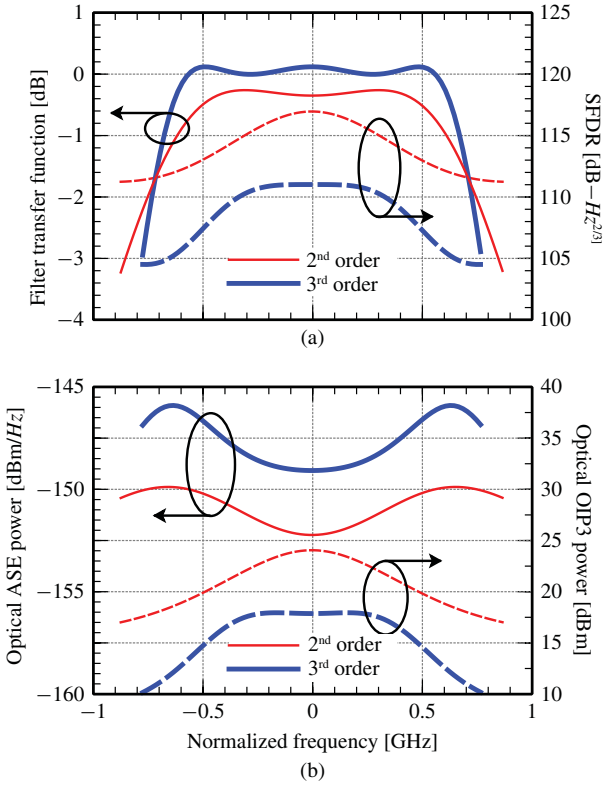

Fig. 8. (a) Second and third-order filter transfer functions and spot-SFDR over the 3 dB bandwidth of the filters. SFDR falls off away from the center of the filter. However, the third-order filter has a wider constant-SFDR plateau that extends for 0.66 GHz with less than 1 dB variation. (b) ASE power and OIP3 power over the 3 dB bandwidth of the second and third-order filters. There is a clear degradation of ASE noise and OIP3 power at the edges of the filter passband.

to the filter shape) as waveguide propagation loss is removed from the forward segment and added to the feedback segment.

1) Second-Order Coupled-Ring Filter: Fig. 4 shows a schematic representation of a second-order coupled ring bandpass filter and Fig. 5 displays the transfer function of a filter across one free spectral range (FSR) with specifications outlined in Table II. A more detailed signal flow diagram can be found in [9]. The filter has a bandwidth of 1.75 GHz, a maximum extinction ratio of 19.8 dB, and a maximum stopband roll-off slope of 11.7 dB/GHz. Like the design described in [9], Mach–Zehnder Interferometer (MZI) tunable couplers comprised of two multi-mode interference (MMI) couplers are modeled between the coupled rings. These allow for complete control of inter-ring coupling. The inter-ring coupling value sets the bandwidth of the filter [9]. Input and output couplers are single MMI couplers. Total ring length is 10 mm, which is split between the couplers and the forward and feedback waveguides of each ring, as given by the feedback to forward ratio in Table II.

With the parameters in Table II, and with all SOAs placed at the end of their respective waveguide segments, there are two remaining degrees of freedom: the distribution of gain between the forward and feedback waveguide segments in the two rings. Fig. 7(a) plots the maximum SFDR in the 3 dB bandwidth of the filter as a function of these two variables. There is a clear maximum when the ring 1 SOA is fully in the feedback segment, and the ring 2 SOA is fully in the forward segment. Intuitively, this can be explained as follows. As seen in Section II-E, IMD is the dominant source of SFDR degradation for an SOA on a waveguide, and the highest SFDR is obtained by limiting the optical power in the SOA. In the example of Section II-E, this is accomplished by placing the SOA at the end of a lossy waveguide. In the second-order coupled ring filter, this is accomplished by placing the ring 1 SOA at the end of the feedback segment. In ring 2, there is no added benefit to placing the SOA in the feedback segment, since the SOA in ring 1 is already the IMD limiting factor. In this case, placing the ring 2 SOA in the feedback segment reduces IMD and ASE at the output, but at the expense of reduced passband gain. Since OIP3 power is proportional to $H_{\mathrm{IO}}^{3/2}$ [Eq. (23)], and the ring 1 SOA is already the IMD limiting factor, the best SFDR is obtained when the ring 2 SOA is placed in the forward segment.

Fig. 7(b) plots the passband gain of the second-order filter as a function of forward/feedback gain distribution in the two rings. The maximum gain is obtained when the SOAs in both rings are fully in the forward segment, but any passband gain between −5.4 dB and +4.9 dB is attainable. The optimal SFDR of 117.0 dB · $\mathrm{Hz}^{2/3}$ is obtained for a passband gain of −0.26 dB. Fig. 6(b) shows this configuration, along with (a) the lowest passband gain configuration, and (c) the highest passband gain configuration. As mentioned in Section III-B,

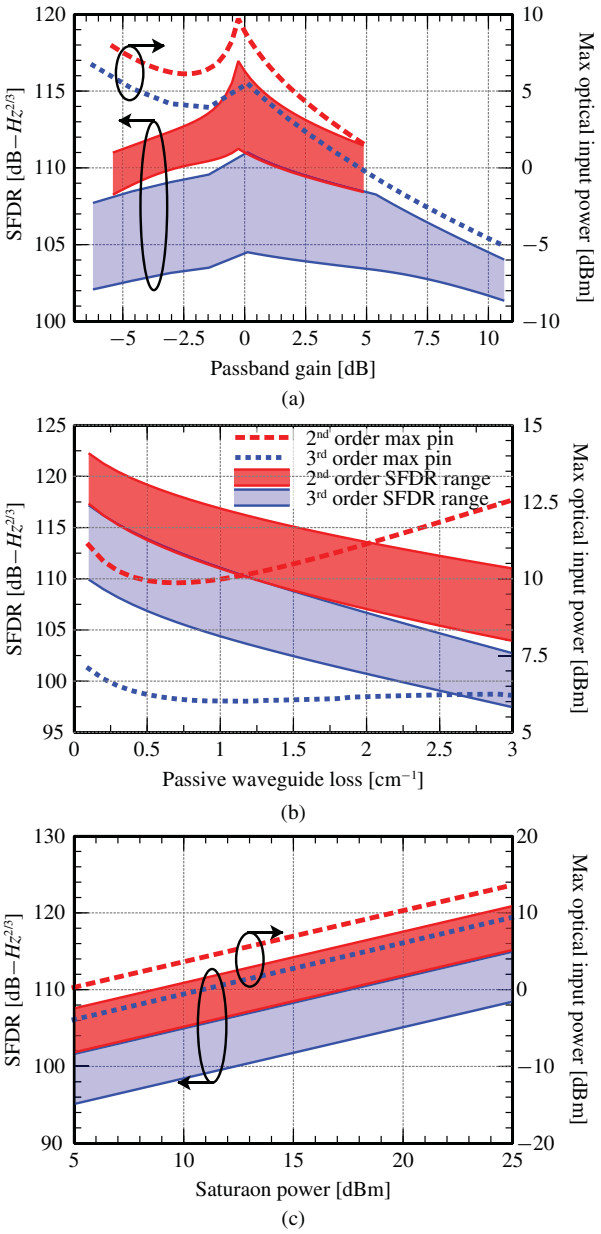

Fig. 9. SFDR range and maximum optical input power (9) seen over the 3 dB bandwidth of the second and third-order filters (a) as a function of passband gain, (b) as a function of passive waveguide loss, and (c) as a function of SOA saturation power. The passband gain is varied by adjusting the distribution of SOA gain in the forward and feedback segments of waveguide in each ring. Since there are multiple ways to achieve each passband gain level, the arrangement that generates the highest SFDR is plotted here. The methods for generating these curves are discussed in Sections III-B.1 and III-B.2. SFDR degrades for both types of filters with increased propagation loss, and increases for increased saturation power. The latter relationship is very simple, and is given by SFDR $\propto P_S^{2/3}$. Continued experimental increases in saturation power and decreases in passive waveguide loss bode well for photonic integrated filters. The integration platform in [15] (and used for all results in this paper) has $\alpha_{ip} = 1$ cm^{-1} and $P_S = 19.1$ dBm.

the passband gain can also be adjusted by varying the feedback to forward waveguide length ratio.

Fig. 8 shows the transfer function, SFDR, OIP3 power, and ASE power as a function of frequency across the 3 dB bandwidth of the filter at the optimal SFDR point. ASE power and IMD power are higher at the edges of the filter (OIP3 power is lower), causing a degradation in the SFDR.

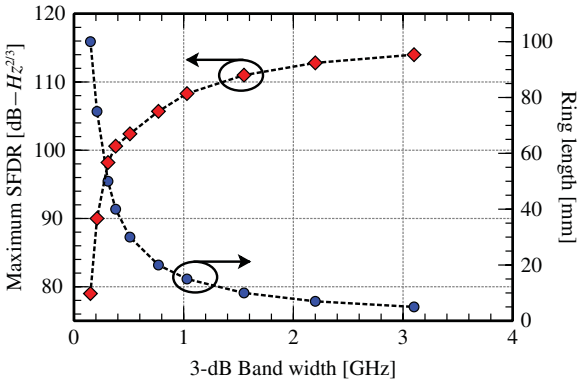

Fig. 10. Maximum SFDR in the 3 dB bandwidth of third-order filters as a function of the bandwidth. Also plotted are the ring lengths needed to reach such bandwidths. SFDR degrades quickly below 1 GHz due to the inverse relationship between ring length and bandwidth. Waveguide propagation loss increases with ring length, negatively impacting SFDR.

Fig. 9 show the effect of varying passband gain, passive waveguide loss, and SOA saturation power on SFDR for both second and third-order filters. The range of SFDR across the 3 dB bandwidth of the filter is plotted along with the optical input power needed to obtain the peak SFDR. In Fig. 9(a), passband gain is varied in such a way as to maximize the SFDR for each point. First, starting with both ring 1 and ring 2 SOA distributions fully in the feedback segment (the point of minimum passband gain), the ring 2 SOA distribution is varied smoothly from fully in the feedback segment to fully in the forward segment. This is the point of maximum SFDR. Then, the ring 1 SOA is varied smoothly from fully in the feedback segment to fully in the forward segment to complete the curve with both ring 1 and ring 2 SOAs fully in the forward segment (the point of maximum passband gain). In Fig. 9(b), (c) as expected, increased passive waveguide loss degrades SFDR, and higher saturation power improves SFDR. The integration platform demonstrated in [15] achieves improvements in both of these parameters over previous active integration platforms with deeply etched waveguides. The maximum input power is high at low loss values because very little gain is needed to compensate for waveguide loss, so very little distortion is generated. However, maximum input power begins to increase again above ~ 1 cm^{-1} because high propagation losses degrade signal power, and higher SOA gain pushes up the noise floor.

2) Third-Order Coupled-Ring Filter: A third-order coupled ring filter with same inter-ring coupling value and ring length as the second-order filter in Section III-B.1 can provide narrower bandwidth, higher extinction, and faster stopband roll-off at the expense of a higher pole magnitude in the center ring [9]. The higher pole magnitude and increased waveguide propagation loss associated with the extra ring result in a degradation in SFDR compared to the second-order filter. Fig. 4 is a schematic representation of a third-order coupled ring filter, and Fig. 5 displays the transfer function of a filter across one FSR with specifications outlined in Table III. Compared with the second-order filter, the extinction ratio is improved by 15.8 dB to 35.6 dB, and the maximum roll-off slope is improved by 16 dB/GHz

to 27.7 dB/GHz. The bandwidth of the third-order filter is 1.55 GHz.

Similarly to the second-order filter, there is an optimal design and passband gain which maximizes the SFDR. Like the second-order design, the SOA in ring 1 is located fully within the feedback segment. To complete the design, the ring 2 SOA is placed fully in the forward segment, and the ring 3 SOA is placed fully in the feedback segment. This provides a passband gain of 0.12 dB and a maxiumum SFDR of 111.0 $\text{dB} \cdot \text{Hz}^{2/3}$. As shown in Fig. 9(a), passband gain can be varied from -6.22 dB to 10.65 dB by adjusting the distribution of SOAs in the rings with a penalty in SFDR. The gain is varied in such a way as to maximize the SFDR for each point, and can be varied further by adjusting the feedback to forward waveguide length ratio. In order to produce Fig. 9(a), for the lowest passband gain, all SOAs were located fully in the feedback segment of their respective rings. Then, the ring 2 SOA is varied smoothly from fully in the feedback segment to fully in the forward segment. This is the arrangement that produces the optimum SFDR. In order to increase passband gain beyond this point, the ring 1 SOA is varied smoothly from fully in the feedback segment to fully in the forward segment. Once this point is reached, the ring 3 SOA distribution is varied in a similar fashion until all SOAs are located fully in the forward segments of their respective rings. This is the point of maximum passband gain.

Fig. 8 shows the transfer function, SFDR, OIP3 power, and ASE power as a function of frequency across the 3 dB bandwidth of the filter at the optimal SFDR point. Like the second-order filter, ASE power and IMD power are higher at the edges of the filter (OIP3 power is lower), causing a degradation in the SFDR. Fig. 9(b), (c) show the effect of variations in passive waveguide loss and SOA saturation power. As expected from substituting Eq. (20) into (21) and the result into (5), SFDR varies linearly with saturation power on a dB-dB scale with a slope of 2/3 for both second and third-order filters.

Fig. 10 shows the variation of SFDR across filters of varying bandwidth. In order to reduce bandwidth, ring lengths are increased, increasing waveguide propagation loss. The resulting reduction in SFDR accelerates below 1 GHz because of the inverse relationship between ring length and bandwidth. Ever more ring length is required to reduce the bandwidth by an appreciable amount. At 0.15 GHz, 100 mm of waveguide is required per ring, degrading SFDR to 79.0 $\text{dB} \cdot \text{Hz}^{2/3}$. With current waveguide propagation loss and saturation power numbers, the active InGaAsP/InP material platform is useful for coupled-ring bandpass filters with bandwidths greater than 1 GHz.

IV. Conclusion

In this paper, we have derived an expression for the PIC-limited SFDR of an RF-photonic link incorporating integrated optical amplifiers in terms of optical powers. The model treats ASE noise, shot noise, and IMD rigorously for a system operating below saturation and in the linear small-signal regime. We have shown simulation results for two systems in particular: second and third-order coupled-ring bandpass filters with 10 mm ring lengths and $\sim$1.75 GHz bandwidths. However, the model presented in Section II-D is applicable to any active analog signal processing system operating in the linear regime. Our examples also utilize results from a new high saturation power integration platform [15]. The results depict trade-offs between filter quality and SFDR performance, with a peak SFDR of 117.0 $\text{dB} \cdot \text{Hz}^{2/3}$ for a second-order filter. A more reasonable third-order filter offering 35.6 dB of extinction results in a peak SFDR of 111.0 $\text{dB} \cdot \text{Hz}^{2/3}$. Recent results measuring the SFDR of RF-photonic links incorporating passive integrated filters are limited to the same range by modulator nonlinearities, link loss, and receiver noise. [2] measures a 105 $\text{dB} \cdot \text{Hz}^{2/3}$ SFDR for a link incorporating an all passive CMOS filter. In their experiment, an attenuator simulates the filter insertion loss in order to avoid excess chip fiber-coupling losses. The filter is assumed to have 6 dB passband insertion loss. [11] also measures a link by substituting an attenuator for a passive filter and reports a maximum SFDR of 108 $\text{dB} \cdot \text{Hz}^{2/3}$ for a link that includes the attenuator and does not use distortion compensation methods. Our results here show that the PIC-limited SFDR of a link incorporating active filters is comparable with that of current passive links. More investigation is required to determine to what extent the modulator nonlinearities, laser RIN noise, and receiver noise of a real link degrade the theoretical PIC-limited SFDR derived in this paper.

Active PIC filters have important advantages over passive filters, including operation without insertion loss or with passband gain, reducing demands on the optical transmitter and receiver. In addition, active filters can synthesize very high quality filter shapes like those in [9]. SOAs are designed to provide the optimal SFDR, but also add an extra element of tuning for "tweaking" filter shapes in-situ. In particular, as filters are tuned in frequency via current-injection phase modulators, loss is introduced via free-carrier absorption. SOA current can be modified in small amounts to retain an optimal shape over the frequency tuning range with negligible effect on SFDR. Continued improvements in passive waveguide loss and SOA saturation power can drive up SFDR such that RF-photonic links are limited by other mechanisms. Practical limits on saturation power in the integration platform discussed here are determined by the trade-off between gain and saturation power, by higher order modes in the transverse direction, and by two-photon absorption [15]. Improvements will need to be made, however, in order to push the SFDR of practical active photonic microwave filters into the 120 $\text{dB} \cdot \text{Hz}^{2/3}$ range required for military radar applications [27]. With the current state of the art in low propagation loss and high saturation power integration platforms, bandpass filters in the InGaAsP/InP material system are limited to bandwidths greater than 1 GHz. For narrower bandwidths, low-loss hybrid-integration platforms such as hybrid InP/Si could provide a solution [8]. For example, with all other parameters kept constant, a reduction in passive waveguide loss by a factor of 10 to 0.1 cm^{-1} would make possible a ten-fold increase in ring length. This would create 0.15 GHz filters with SFDR equal to the 1.55 GHz filters presented here (see Fig. 10).

The ability to implement other active components on-chip along side optical signal processing circuits continues to make the active InGaAsP/InP material system interesting for RF-photonics. Active material systems also provide design versatility that is not possible with passive filters. With a high saturation power material platform and optimal SFDR design, active photonic integrated circuits can provide high quality and high fidelity signal processing for RF-photonic systems.

REFERENCES

[1] J. Yao, "Microwave photonics," *J. Lightw. Technol.*, vol. 27, no. 3, pp. 314–335, Feb. 2009.

[2] K.-Y. Tu, M. S. Rasras, D. M. Gill, S. S. Patel, Y.-K. Chen, A. E. White, A. Pomerene, D. Carothers, J. Beattie, M. Beals, J. Michel, and L. C. Kimerling, "Silicon RF-photonic filter and down-converter," *J. Lightw. Technol.*, vol. 28, no. 20, pp. 3019–3028, Oct. 2010.

[3] T. K. Woodward, T. C. Banwell, A. Agarwal, P. Toliver, and R. Menendez, "Signal processing in analog optical links," in *Proc. IEEE Conf. Avionics Fiber-Opt. Photon. Technol.*, San Antonio, TX, 2009, pp. 17–18.

[4] J. Capmany, B. Ortega, and D. Pastor, "A tutorial on microwave photonic filters," *J. Lightw. Technol.*, vol. 24, no. 1, pp. 201–229, Jan. 2006.

[5] M. S. Rasras, D. M. Gill, S. S. Patel, K.-Y. Tu, Y.-K. Chen, A. E. White, A. T. S. Pomerene, D. N. Carothers, M. J. Grove, D. K. Sparacin, J. Michel, M. A. Beals, and L. C. Kimerling, "Demonstration of a fourth-order pole-zero optical filter integrated using CMOS processes," *J. Lightw. Technol.*, vol. 25, no. 1, pp. 87–92, 2007.

[6] N.-N. Feng, P. Dong, D. Feng, W. Qian, H. Liang, D. C. Lee, J. B. Luff, A. Agarwal, T. Banwell, R. Menendez, P. Toliver, T. K. Woodward, and M. Asghari, "Thermally-efficient reconfigurable narrowband RF-photonic filter," *Opt. Express*, vol. 18, no. 24, pp. 24648–24653, 2010.

[7] P. Dong, N.-N. Feng, D. Feng, W. Qian, H. Liang, D. C. Lee, B. J. Luff, T. Banwell, A. Agarwal, P. Toliver, R. Menendez, T. K. Woodward, and M. Asghari, "Ghz-bandwidth optical filters based on high-order silicon ring resonators," *Opt. Express*, vol. 18, no. 23, pp. 23784–23789, 2010.

[8] H.-W. Chen, A. Fang, J. D. Peters, Z. Wang, J. Bovington, D. Liang, and J. Bowers, "Integrated microwave photonic filter on a hybrid silicon platform," *IEEE Trans. Microw. Theory Tech.*, vol. 58, no. 11, pp. 3213–3219, Nov. 2010.

[9] R. S. Guzzon, E. J. Norberg, J. S. Parker, L. A. Johansson, and L. A. Coldren, "Integrated InP-InGaAsP tunable coupled ring optical bandpass filters with zero insertion loss," *Opt. Express*, vol. 19, no. 8, pp. 7816–7826, 2011.

[10] E. J. Norberg, R. S. Guzzon, J. Parker, L. A. Johansson, and L. A. Coldren, "Programmable photonic microwave filters monolithically integrated in InPInGaAsP," *J. Lightw. Technol.*, vol. 29, no. 11, pp. 1611–1619, Jun. 2011.

[11] A. Agarwal, T. Banwell, and T. K. Woodward, "Optically filtered microwave photonic links for RF signal processing applications," *J. Lightw. Technol.*, vol. 29, no. 16, pp. 2394–2401, Aug. 2011.

[12] T. Numai, *Laser Diodes and Their Applications to Communications and Information Processing*. New York: Wiley, 2010.

[13] R. M. Jopson and T. E. Darcie, *Coherence, Amplification, and Quantum Effects in Semiconductor Lasers*, Y. Yamamoto, Ed. New York: Wiley, 1991.

[14] P. Berger, J. Bourderionnet, M. Alouini, F. Bretenaker, and D. Dolfi, "Theoretical study of the spurious-free dynamic range of a tunable delay line based on slow light in SOA," *Opt. Express*, vol. 17, no. 22, pp. 20584–20597, 2009.

[15] E. Norberg, R. S. Guzzon, J. S. Parker, S. DenBaars, and L. Coldren, "An InGaAsP/InP integration platform with low loss deeply etched waveguides and record SOA RF-linearity," in *Proc. Eur. Conf. Opt. Commun.*, Geneva, Switzerland, Sep. 2011, pp. 1–3.

[16] J. Lerdworatawee and W. Namgoong, "Revisiting spurious-free dynamic range of communication receivers," *IEEE Trans. Circuits Syst I*, vol. 53, no. 4, pp. 937–943, Apr. 2006.

[17] D. M. Baney, P. Gallion, and R. S. Tucker, "Theory and measurement techniques for the noise figure of optical amplifiers," *Opt. Fiber Technol.*, vol. 6, no. 2, pp. 122–154, 2000.

[18] G. P. Agrawal, "Population pulsations and nondegenerate four-wave mixing in semiconductor lasers and amplifiers," *J. Opt. Soc. Amer. B*, vol. 5, no. 1, pp. 147–159, 1988.

[19] T. E. Darcie and R. M. Jopson, "Nonlinear interactions in optical amplifiers for multifrequency lightwave systems," *Electron. Lett.*, vol. 24, no. 10, pp. 638–640, May 1988.

[20] Y. C. Chung, J. M. Wiesenfeld, G. Raybon, U. Koren, and Y. Twu, "Intermodulation distortion in a multiple-quantum-well semiconductor optical amplifier," *Photon. Technol. Lett.*, vol. 3, no. 2, pp. 130–132, Feb. 1991.

[21] M. J. Adams, D. A. O. Davies, M. C. Tatham, and M. A. Fisher, "Nonlinearities in semiconductor laser amplifiers," *Opt. Quantum Electron.*, vol. 27, no. 1, pp. 1–13, Jan. 1995.

[22] T. Marozsak, E. Udvary, and T. Berceli, "Transmission characteristics of all semiconductor fiber optic links carrying microwave channels," in *Proc. Eur. Microw. Conf.*, Oct. 2000, pp. 1–4.

[23] C. K. Madsen and J. H. Zhao, *Optical Filter Design and Analysis: A Signal Processing Approach*. New York: Wiley 1999.

[24] P. Saeung and P. P. Yupapin, "Generalized analysis of multiple ring resonator filters: Modeling by using graphical approach," *Optik Int. J. Light Electron Opt.*, vol. 119, no. 10, pp. 465–472, Aug. 2008.

[25] T. Saitoh and T. Mukai, *Coherence, Amplification, and Quantum Effects in Semiconductor Lasers*, Y. Yamamoto, Ed. New York: Wiley, 1991.

[26] M. Osinski and J. Buus, "Linewidth broadening factor in semiconductor lasers–an overview," *IEEE J. Quantum Electron.*, vol. 23, no. 1, pp. 9–29, Jan. 1987.

[27] J. Choe, "Defense RF systems: Future needs, requirements, and opportunities for photonics," in *Proc. IEEE Conf. Microw. Photon.*, 2005, pp. 307–310.

Robert S. Guzzon received the B.S. degree in electrical engineering and physics from Lehigh University, Bethlehem, PA, in 2007. He is currently pursuing the Ph.D. degree in electrical engineering with the University of California, Santa Barbara.

His current research interests include the design and fabrication of versatile photonic integrated microwave filter systems that achieve high spurious free dynamic range, large-scale photonic integration, and microwave photonic signal processing.

Erik J. Norberg received the B.S. and M.S. degrees in engineering nanoscience from Lund University, Lund, Sweden, in 2008. He is currently pursuing the Ph.D. degree in electrical engineering with the University of California, Santa Barbara.

He is currently working on the development of high dynamic range integrated optical filters for microwave signal processing. His current research interests include the design and metal organic chemical vapor deposition growth of large scale photonic integrated circuits on InP.

Larry A. Coldren (F'82) received the Ph.D. degree in electrical engineering from Stanford University, Stanford, CA, in 1972.

He is the Fred Kavli Professor of optoelectronics and sensors and the Acting Richard A. Auhll Dean of engineering with the University of California, Santa Barbara (UCSB). After 13 years in the research area with Bell Laboratories, Holmdel, NJ, he joined UCSB in 1984, where he is currently with the Department of Materials and the Department of Electrical and Computer Engineering. In 1990, he co-founded optical concepts, later acquired as Gore Photonics, to develop novel vertical-cavity surface-emitting laser (VCSEL) technology, and in 1998, he co-founded Agility Communications, Inc., Goleta, CA, later acquired by JDS Uniphase Corporation (JDSU), Milpitas, CA, to develop widely tunable integrated transmitters. At Bell Laboratories, he was initially on waveguided surface-acoustic-wave signal processing devices and coupled-resonator filters. He later developed tunable coupled-cavity lasers using novel reactive-ion etching technology that he created for the new InP-based materials. At UCSB, he continued work on multiple-section tunable lasers, in 1988, inventing the widely tunable multi-element mirror concept, which is currently used in some JDSU products. Near this same time period, he also made seminal contributions to efficient VCSEL designs that continue to be implemented in practical devices to present. More recently, his group has developed high-performance InP-based photonic integrated circuits as well as high-speed VCSELs, and they continue to advance the underlying materials growth and fabrication technologies. He has authored or co-authored over 1000 journals and conference papers, seven book chapters, and one textbook and has been issued 63 patents. He has presented dozens of invited and plenary talks at major conferences.

Prof. Coldren is a member of the National Academy of Engineering. He was a recipient of the John Tyndall and the Aron Kressel Awards in 2004 and 2009, respectively.